Biomaterials Advances 176 (2025) 214340

Contents lists available at ScienceDirect

Biomaterials Advances

journal homepage: www.journals.elsevier.com/materials-science-and-engineering-c

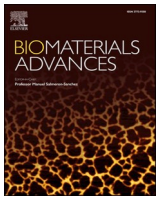

Engineered bioactive glass-chitosan hybrid for dual tissue and bone regeneration multifunctional healing

Yu-Chien Lin [a,b,1], Susaritha Ramanathan [a,1], Huey-Yuan Wang [c,1], Ying-Chun Lin [a], Wai-Ching Liu [d], Julian R. Jones [e], Nam-Joon Cho [b,f,*], Chih-Chien Hu [g,**], Ren-Jei Chung [a,h,***]

[a] Department of Chemical Engineering and Biotechnology, National Taipei University of Technology, Taipei, Taiwan
[b] School of Materials Science and Engineering, Nanyang Technological University, Singapore
[c] Department of Stomatology, MacKay Memorial Hospital, Taipei, Taiwan
[d] Department of Food and Health Sciences, Technological and Higher Education Institute of Hong Kong, Hong Kong, China
[e] Department of Materials, Imperial College London, London, UK
[f] Centre for Cross Economy Global, Nanyang Technological University, Singapore
[g] Bone and Joint Research Center, Chang Gung Memorial Hospital, Taiwan
[h] High-value Biomaterials Research and Commercialization Center, National Taipei University of Technology (Taipei Tech), Taipei 10608, Taiwan

ARTICLE INFO

Keywords:
Chitosan-silica hybrid
Wound dressing
Bioactive glass
Biodegradable
Bone regeneration

ABSTRACT

The treatment of complex wounds, particularly those arising from conditions such as diabetes or trauma, presents a significant clinical challenge. These wounds often necessitate long-term care for soft tissue and bone repair, creating an urgent need for multifunctional wound dressings. This study introduces a chitosan-silica hybrid dressing enhanced with bioactive glass (BG), specifically designed to address this need. The hybrid material achieves molecular bonding through coupling agents, with the organic chitosan component providing swelling and hemostatic effects, while the inorganic silica and BG release ions (Si^{4+}, Ca^{2+}), promoting tissue regeneration and bone healing. With a controlled degradation profile (lasting 3 to 6 months *in-vitro*), the dressing is ideal for chronic wound management. Experimental results demonstrate excellent biocompatibility, no inflammatory response, and strong hemostatic properties due to the positively charged chitosan and cations. Adding BG significantly enhances bone regeneration, positioning this chitosan-silica hybrid as a promising solution for the simultaneous repair of soft tissue and bone.

1. Introduction

Traditional wound dressings, such as gauze, breathable films, foams, hydrogels, hydrocolloids, and bandages, were originally designed to absorb exudate and maintain a moist environment, providing an essential barrier against microbial invasion [1]. While these dressings support the natural physiological healing process, their role is primarily passive, offering minimal contribution to wound repair beyond protection and exudate management [2,3]. Their ease of application and removal makes them convenient for clinical use, but they fall short in promoting complex healing processes, especially for more severe or chronic wounds [4]. The emergence of next-generation bioactive wound dressings seeks to address these limitations by actively participating in the wound regeneration process. These advanced dressings, often incorporating natural polymers such as alginate, chitosan, chitin, and collagen, have demonstrated significant potential in enhancing soft tissue repair [5,6]. By leveraging the intrinsic bioactive properties of these materials, bioactive dressings can create a more conducive environment for cellular growth, inflammation control, and the overall acceleration of tissue repair processes [7]. Hydrogels, in particular, have gained significant attention due to their tunable mechanical properties, biocompatibility, and capacity to provide sustained release of bioactive agents. However, while these natural polymers excel in soft tissue regeneration, their capacity to support bone tissue healing remains

* Correspondence to: N.-J. Cho, School of Materials Science and Engineering, Nanyang Technological University, 50 Nanyang Avenue, Singapore 639798, Singapore.
** Correspondence to: C.-C. Hu, Bone and Joint Research Center, Chang Gung Memorial Hospital, Taiwan
*** Correspondence to: R.-J. Chung, Department of Chemical Engineering and Biotechnology, National Taipei University of Technology, Taipei, Taiwan.
E-mail addresses: njcho@ntu.edu.sg (N.-J. Cho), r52906154@cgmh.org.tw (C.-C. Hu), rjchung@mail.ntut.edu.tw (R.-J. Chung).
[1] These authors contributed equally to this paper.

https://doi.org/10.1016/j.bioadv.2025.214340
Received 27 February 2025; Received in revised form 1 May 2025; Accepted 6 May 2025
Available online 8 May 2025

limited. Bone tissue formation is a more complex and prolonged process, requiring the deposition of inorganic ions like calcium and phosphate to initiate the mineralization needed for bone formation. This involves a highly orchestrated series of cellular interactions that lead to the development of bone apatite, a process that natural polymers alone may not adequately support. Recent advancements in wound dressing technology have focused on creating multifunctional dressings that can address soft tissue and bone regeneration.

The development of wound dressings and scaffolds for tissue regeneration has long relied on hydrogel-based systems due to their high water content, biocompatibility, and adaptability [8] Hydrogels, with their tunable degradation rates, have also been explored as vehicles for delivering bioactive molecules and inorganic components such as bioactive glass (BG) or ceramics to enhance bone regeneration [9]. However, conventional chitosan-based hydrogels typically employ dynamic covalent crosslinking (*e.g.*, imine bonds from furfural or glutaraldehyde) [10,11], secondary photoinitiated mechanisms (*e.g.*, UV-triggered PEG-NHS reactions) [12], which yield elastic and adhesive materials suitable for short-term applications. These dynamic or reversible crosslinking strategies are inherently susceptible to hydrolytic degradation in aqueous or physiological environments, leading to rapid mechanical deterioration and limited structural longevity [6,8]. Even when reinforced with secondary curing or functional agents such as hydrogen sulfide-releasing moieties or photothermal compounds, their compressive strength commonly remains below 200 kPa, restricting their applicability in load-bearing or long-duration wound healing scenarios [12].

In contrast, organic–inorganic hybrid systems, particularly those employing silane coupling agents like (3-Glycidyloxypropyl)trimethoxysilane (GPTMS), form covalently bonded silica networks within the organic polymer matrix. Unlike traditional composites, these hybrids achieve molecular-level integration, resulting in a single-phase material with controlled, homogeneous degradation [13,14]. Previous studies have shown that incorporating <10 wt% SiO_2 into a gelatin or chitosan matrix *via* silane coupling significantly improves structural stability [15], as the silane epoxide groups bond with the organic chains while the methoxysilane moieties undergo polycondensation to form a robust silica framework [14]. This architecture avoids the weak points and rapid breakdown observed in purely organic systems [16]. Moreover, the incorporation of bioactive glass provides a sustained release of biologically active ions such as Si^{4+} and Ca^{2+}, which can promote both soft tissue healing and bone regeneration [17] For instance, GPTMS-crosslinked chitosan-silica hybrids supplemented with tetraethyl orthosilicate (TEOS) and BG have demonstrated compressive moduli approaching 400 kPa, maintaining shape fidelity and ion release under physiological conditions for over three months. Compared to hydrogels that often disintegrate within days to weeks, these hybrid materials offer superior mechanical resilience and functional longevity, making them highly promising for the treatment of complex or chronic wounds requiring dual tissue and bone regeneration [18].

In this study, we present a BG-containing chitosan-silica hybrid dressing, designed to address the challenges of prolonged treatment for both soft and hard tissue repair, as illustrated in Fig. 1. By incorporating BG, the multifunctional dressing not only promotes soft tissue healing but also supports the bone regeneration process. The hybrid structure ensures a controlled degradation rate, extending the dressing's effectiveness and allowing for the simultaneous regeneration of both soft and hard tissues. This makes it a promising solution for treating complex wounds, such as those associated with osseous injuries or chronic diabetic wounds.

2. Materials and methods

2.1. Materials

All chemicals and solvents were purchased from J.T. Baker (USA), unless otherwise specified. Dulbecco's Modified Eagle's Medium (DMEM) and alpha-medium (α-MEM) were obtained from Invitrogen, Thermo Fisher Scientific, USA. Chitosan (medium molecular weight (Mw), ≥ 75 % deacetylated), TEOS, GPTMS, 3-[(Ethylimino)methylidene]amino-*N*,*N*-dimethylpropan-1-amine (EDC), N-Hydroxysuccinimide (NHS), and Cell Counting Kit-8 (CCK-8) were acquired from Sigma, USA.

2.2. Preparation of chitosan-silica hybrid

Chitosan undergoes an initial reaction with GPTMS. Initially, 0.6 g of chitosan is added to 20 mL of deionized (DI) water with 0.2 mL of acetic acid solution, stirred at 400 rpm for approximately 10 min until no impurities are observed. Subsequently, 0.5 mL of GPTMS is added, and stirring is continued for another 10 min. Following this, 0.0825 g of EDC and 0.04125 g of NHS are added and mixed for 4 h. Afterward, an organic solution is obtained. Separately, inorganic solution is obtained by mixing 0.045, 0.09, or 0.135 mL of TEOS in 0.89 mL of deionized water with 0.3 mL of 0.5 M hydrochloric acid (HCl), stirring at 400 rpm for 1 h. Gradually add the inorganic solution dropwise into a beaker containing the organic solution and stir for 1 day. Afterward, leave it in a dialysis bag for 3 days and freeze-dry to obtain the sample. The materials have TEOS/chitosan (T/C) concentrations of 10 wt% TEOS to 90 wt% chitosan (10 T/C), 20 T/C, and 30 T/C, respectively.

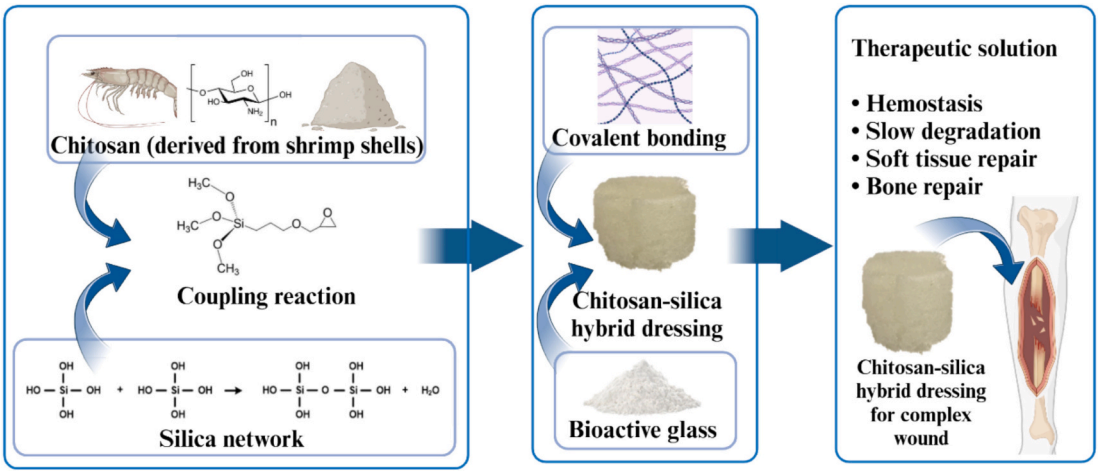

Fig. 1. This study synthesized a chitosan-silica hybrid using a coupling reaction, forming covalent bonds between chitosan and the silica network, and incorporated bioactive glass to create a multifunctional dressing for complex wound applications.

2.3. Preparation of bioactive glass containing chitosan-silica hybrid

This study utilized BG with synthetic components previously employed in research and employed the sol-gel synthesis method [19]. In summary, TEOS, calcium nitrate tetrahydrate, and triethyl phosphate, with a molar ratio of Si: Ca: P = 60: 35: 5, were dissolved in 1.00 g of 0.5 M HCl, 30.00 mL of 95 % ethanol, and 30.00 mL of DI water. The mixture was stirred at room temperature for 1 h to create a homogeneous precursor solution. The solution was then sealed with a lid and placed in a 60 °C oven for aging for 24 h. The precursor solution underwent a sol-gel transition, resulting in a gel-like state. The lid was opened to allow solvent evaporation in a 60 °C oven for an additional 24 h. The solid precursor was transferred to a furnace (Muffle Furnace DFH-20, DENGYNG, Taiwan) and sintered with a heating rate of 10 °C/min, calcination at 650 °C for 1 h. The power was then shut down, allowing the material to cool to room temperature in the furnace. The sintered BG was subjected to ball milling (Spex SamplePrep 8000 M Mixer Mill, USA) using a mixture of zirconia balls with diameters of 2 and 10 mm at a rotation speed of 1425 rpm for 12 h. The resulting mixture was then sieved through a 150 μm mesh to obtain BG powder.

For the chitosan-silica hybrid mixed with BG, a 30 T/C ratio was chosen for further experimentation. 5 wt% of BG (30 T/C-5%B) was mixed into 30 T/C immediately after the additional hydrolyzed TEOS in the chitosan solution, as mentioned in Section 2.2. The subsequent steps were identical to those for 30 T/C. After freeze-drying, the samples were ready for further experimentation.

2.4. Material characterization

For material characterization, chitosan-silica hybrids were examined for both chemical and physical properties. The chemical structures of the chitosan-silica hybrids were assessed using attenuated total reflection-Fourier-transform infrared spectroscopy (ATR-FTIR, Spotlight 200i Sp2 with AutoATR System, Perkin Elmer, USA). The measurements were conducted within a range of 4000 to 500 cm^{-1}. Additionally, ^{1}H nuclear magnetic resonance (NMR, 400 MHz Spectrometer, JEOL, Japan) was employed to demonstrate changes in the chemical structure before and after the coupling reaction. Precursors were dissolved in deuterated chloroform $CDCl_3$ to achieve a final concentration of 10 mg/mL for NMR analysis.

Freeze-dried scaffolds, shaped as 1 cm^3 cubes, were utilized for swelling, water retention, and degradation experiments. In the swelling test, the initial weight of the freeze-dried scaffold (W_{dry}) was recorded, and the sample was then immersed in phosphate-buffered saline (PBS). The weight of the wet scaffold (W_{wet}) was measured at different time points. The swelling ratio (%) was calculated as follow:

$$\text{Swelling ratio } (\%) = \frac{(W_{wet} - W_{dry})}{(W_{dry})} \times 100\%$$

For water retention, dried scaffolds were weighed (W_{dry}) and immersed in deionized water for 1 h. The weight of the wet scaffolds (W_{wet}) was measured at different time points up to 8 h. Water retention (%) was calculated as follow:

$$\text{Water rentetion } (\%) = \frac{(W_{wet} - W_{dry})}{(W_{dry})} \times 100\%$$

The degradation test involved soaking dried scaffolds in PBS at 37 °C for a specific duration and measuring the weight loss afterward. The initial weight of the dried scaffolds (W_0) was recorded. After immersing the samples in PBS for various durations, the samples were retrieved at different time points, and the weight of the freeze-dried scaffolds (W_1) was measured to obtain the degraded weight. The degradation rate (%) was calculated as follow:

$$\text{Water rentetion } (\%) = \frac{(W_0 - W_1)}{(W_0)} \times 100\%$$

To screen silicon ion release during degradation, inductively coupled plasma-optical emission spectrometry (ICP-OES, Optima 8000, PerkinElmer, USA) was employed to test the degradation solution. Thermogravimetric analysis (TGA, STA7300, HITACHI, Japan) was utilized to determine the individual weight percentages of organic and inorganic compounds. The surface morphology, microstructure, and element distribution of the scaffold were investigated using scanning electron microscopy (SEM, Phenom XL G2, Thermo Scientific, USA) with energy dispersive X-ray (EDX, JEOL, JEM2100F) detector, after sputtering the samples with Au. Finally, the surface charge of the scaffold was evaluated using a Zeta sizer (Nano series, Malvern, Taiwan).

2.5. Cell viability

All cell lines were procured from American Type Culture Collection (ATCC, USA). L929, a mouse fibroblast cell line, and rat bone marrow mesenchymal stem cells (rBMSCs) were chosen as models for investigating cell-material interactions. L929 cells were cultured in DMEM, while rBMSCs were cultured in minimum essential α-MEM, both at 37 °C in a 5 % CO_2 environment. rBMSCs, being stem cells, were also used for testing alkaline phosphatase activity (ALP) as a potential osteogenic biomarker. In this study, the biocompatibility of chitosan-silica hybrids was initially assessed using the L929 cell line. Samples were labeled as chitosan, 10 T/C, 20 T/C, and 30 T/C. The optimal condition, 30 T/C, was selected for further experimentation, including 30 T/C-5%B. These samples were co-cultured with rBMSCs for cell viability and additional cellular response evaluations.

Cell biocompatibility tests were performed using a CCK-8 assay on L929 and rBMSCs cell lines. Samples were sterilized with ultraviolet (UV) light for 30 min and then placed in 15 mL centrifuge tubes at concentrations of 0 (control), 0.5, 1, 2.5, and 5 mg/mL in culture medium for sample extraction preparation at 37 ± 1 °C for 72 ± 2 h. The evaluation adhered to the International Organization for Standardization (ISO 10993-12:2012) guidelines for the biological evaluation of medical devices. Each well plate was seeded with 2.5×10^4 cells containing 200 μL of the extraction medium for two days. After washing the well plate three times with PBS, a mixture of 200 μL CCK-8 reaction reagent and clean medium (in a ratio of 1:9) was added to each well in the dark for 2 h in the 37 °C incubator. Following the completion of the reaction, the clean medium was transferred to a new 96-well plate, and a multimode microplate reader (MMR, VarioskanTM FLASH, Thermo, USA) was used to measure the absorbance (abs.) at a wavelength of 450 nm. Cell viability (%) was calculated as follow:

$$\text{Cell viability } (\%) = \frac{(Abs.of\ sample - Abs.of\ blank)}{(Abs.of\ control - Abs.of\ blank)} \times 100\%$$

2.6. Alkaline phosphatase activity (ALP) test

The substrate buffer solution was for degradation rate ted by combining 0.1856 g of 4-nitrophenol powder, 0.4845 mL of 2-amino-2-methyl-1-propanol, and 0.0407 g of magnesium chloride hexahydrate ($MgCl_2{\cdot}6H_2O$) in 100 mL DI water. Subsequently, the substrate buffer was diluted to a specific concentration for ALP standard measurement, ranging from 20,000 to 0 μM, using DI water. The concentration of the ALP standard was assessed using UV–vis (SP-8001, Yoyu, Taiwan) at an abs. of 450 nm. For the ALP experiments, rBMSCs at a density of 5×10^4 cells were co-cultured with the extracted solutions, as described in Section 2.5, for 1, 3, 7, and 14 days. The co-culture α-MEM medium was collected and mixed with 500 μL of 0.1 % Triton X-100 dissolved in 0.1 M Tris buffer. The mixture was evenly blended by ultrasonication for 10 min. A 50 μL aliquot of the prepared solution was mixed with 200 μL of the substrate buffer and allowed to react for 60 min in a 96-well plate.

The reaction was terminated by adding 100 μL of 1 N NaOH solution. Finally, the ALP activity was measured using UV–Vis at 405 nm.

2.7. Cell migration wound healing assay

The *in-vitro* wound healing assay aimed to mimic cell migration at a wound site, with faster cell migration and coverage of the entire wound area indicating accelerated wound healing. Extracts from chitosan-silica hybrid scaffolds, collected as mentioned in Section 2.5, were used as the sample extraction medium. In a 6-well plate, 1×10^4/mL L929 cells were cultured using clean medium for 24 h to ensure homogeneous coverage of the plate surface by the cells. After removing the clean medium, the wells were washed with PBS three times, and 1 mg/mL of the sample extraction was added. A horizontal scratch, spaced 5 mm apart, was made in each well using a 1000 μL tip, along with a vertical cut following the marked line when the cell density exceeded 90 %. The plate was then placed in a 37 °C, 5 % CO_2 incubator for 0, 4, 8, 12, and 24 h. Pictures were taken at each time point using an optical microscope to observe the progression of cell migration. The migration area was calculated using Image J software.

2.8. In-vivo wound closure test

All animal experiments and care were ethically approved by Laboratory Animal Center of Taipei Medical University (LAC-2022-0203) and Chang Gung Memorial Hospital, Linkou (IACUC No: 2023030305) (n = 3 for each group), Taiwan, using 6-week-old Sprague Dawley (SD) rats. Experimental groups included a control group with wounds left untreated, a group treated with 30 T/C dressing, and a group treated with 30 T/C-5%B (n = 3 for each group). To prepare the anesthetic, Zoletil 50 and Rompun 20 were mixed in a 1: 2 ratio and injected intraperitoneally into the SD rats at 0.1 mL of anesthetic solution per 100 g of rat weight. The backs of the SD rats were shaved, and the planned surgical site was cleaned with 70 % ethanol. A circular wound with a diameter of 2.5 cm was cut on the rat's back using a surgical scalpel and scissors. Samples, shaped as 2.5 cm disks with a thickness of 1 mm, were placed on the wound site. Subsequently, an artificial skin (TegadermTM film, 3 M health care, USA) was applied over the wound, and an o-ring was placed and sutured together with the surrounding skin to securely affix the sample to the wound site. Wound healing progress was observed on days 7, 14, and 21, and Image J software was utilized to analyze the wound healing area. Finally, euthanasia was performed using CO_2, and the skin at the wound site was harvested and fixed in formalin. Toson Technology Co. Ltd. conducted Masson's trichrome staining procedures in Taiwan. Optical microscopy was then employed to capture images of the stained samples.

2.9. In-vivo hemostasis studies

The *in-vivo* hemostasis study used the rat liver puncture method [20]. Rats were administered anesthesia *via* intraperitoneal injection, and the sacrifice steps followed the same procedure as outlined in Section 2.7. The abdominal region of the rat was incised along the lower edge of the rib arch to expose the liver using sterilized surgical tools. A 47 mm diameter Whatman® polycarbonate filter was placed beneath the liver. Liver injury was induced using a 5 mm diameter biopsy punch, creating a wound about 5 mm in depth. In the blood loss experiments, the filter and all samples, including gauze, 30 T/C, and 30 T/C-5%B, were pre-weighed to 1 g and prepared for the experiment. After inducing the injury, samples were applied to the wound site with minimal pressure, and the resulting mass was immediately recorded. Bleeding times were also recorded simultaneously.

2.10. In-vivo cranial defect experiment for bone regeneration

The cranial defect experiment was employed to assess bone regeneration. Rats were categorized into three groups: the control group with an empty defect, 30 T/C, and 30 T/C-5%B. The anesthesia process and related hair removal steps followed the previously outlined procedure, and the surgical site was disinfected using 70 % ethanol. A 5 mm skull defect was created using a microdrill, with physiological saline used during the procedure for cooling and maintaining eye moisture. Samples, shaped as 5 mm in diameter and 1 mm in height, were prepared to fit into the skull defect. No additional fixation materials were used, and absorbable sutures were employed to close the wound. Skull repair progress was observed on 2 and 4 weeks post-surgery, and computer tomography (CT, nanoScan® PET/CT) was utilized to display the cranial repair status. ImageJ was then used to reconstruct 3D models and calculate bone volume/total volume (BT/TV) ratio. After the final round of CT scanning, euthanasia was performed using CO_2, and the bones around the skull defect were extracted and fixed in formalin. Hematoxylin and Eosin (H&E), as well as Masson staining procedures, were carried out by Toson Technology Co. Ltd. in Taiwan. Subsequently, scanning images were used to analyze the stained samples.

2.11. Statistical analysis

The data collected in this study underwent statistical analysis using Origin software. Group differences in numerical values were assessed through the Tukey test. All experiments adhered to a completely random design. Significant differences in the data were denoted as $^*p < 0.05$, highly substantial differences as $^{**}p < 0.01$, and very highly significant differences as $^{***}p < 0.001$. In cases where the differences between two sets of data were not important, it was indicated as $p > 0.05$.

3. Results and discussion

3.1. Chemical characterization of chitosan-silica hybrid

In terms of the chemical characterization of the chitosan-silica hybrid, Nuclear magnetic resonance spectroscopy (NMR) results are presented in Fig. 2(a) and (b) to observe changes in chemical structures before and after the coupling reaction. Fig. 2(a) displays the corresponding chemical shifts of GPTMS as labeled. The key aspect is the identification of the ring-opening reaction of GPTMS, achieved by monitoring the peaks labeled ‘g’ at 2.5 ppm and ‘g’ at 2.7 ppm, representing the epoxy group as indicated in the blue zone. Following the ring-opening reaction [20], the NMR results of the chitosan-silica hybrid in Fig. 2(b) indicate a significant decrease in peak intensities at 2.5 and 2.7 ppm, suggesting successful opening of the epoxy ring on the GPTMS. Additionally, the hybrid NMR results suggest the presence of acetyl and CH_3 groups, indicating successful conjugation of GPTMS with chitosan. On the other hand, the peaks corresponding to the silanol groups are highlighted in the yellow zone, demonstrating significant changes due to the polycondensation reaction of the silanol groups with the hydrolyzed silica network by TEOS.

The hybrid materials have been synthesized by controlling TEOS/chitosan (T/C) concentrations of 10 wt% TEOS to 90 wt% chitosan (10 T/C), 20 T/C, 30 T/C, and 30 T/C with 5 % BG (30 T/C-5%B) respectively. In Fig. 2(c), the Fourier transform infrared spectroscopy (FTIR) detection results show a broad band around 1040 and 1070 cm^{-1}, indicative of Si-O-Si signals, is observed for TEOS [21]. However, in chitosan, within the similar range of 1030 and 1070 cm^{-1}, two wavelength ranges show C—O skeleton vibrations, with the most prominent characteristic peaks overlapping with them. Subsequently, at 1150 cm^{-1}, there is the presence of –C–O–C– of glycosidic linkage, along with characteristic absorption bands at 1640 cm^{-1} (C═N stretching vibration of the imine group), 1546 cm^{-1} (–NH_2 bending), and 1382 cm^{-1} (C═N bending) [21–23].

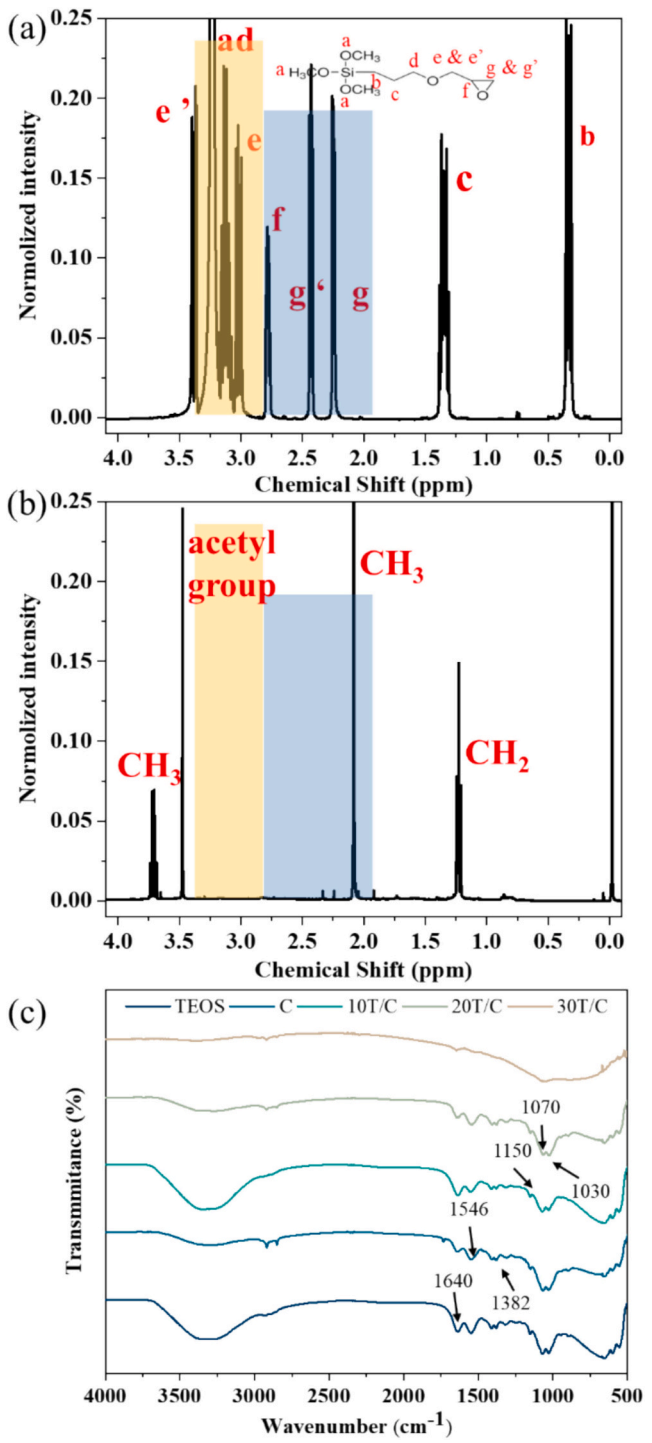

Fig. 2. (a) The ^{1}H NMR spectrum data of GPTMS shows the positions marked as a–g′ corresponding to the chemical structure of GPTMS. (b) The ^{1}H NMR spectrum of the chitosan-silica hybrid displays the chemical structure, with yellow and blue regions corresponding to the emphasized peak shifts in (a). (c) FTIR spectra display the data for the TEOS precursor and chitosan-silica hybrid materials with varying TEOS ratios. 'C' represents pure chitosan, while '10T/C' indicates a hybrid with 10 wt% TEOS relative to chitosan, with a similar notation applied for other TEOS concentrations.

3.2. Physical properties characterization of chitosan-silica hybrid

After undergoing the coupling reaction, the chitosan-silica hybrid transitions from a relatively loose morphology to a more compact scaffold. A SEM was used to observe changes in surface morphology, and EDX was utilized for elemental mapping to determine the distribution of elements. As depicted in Fig. 3, the chitosan sample exhibits a loose structure, forming a mesh-like network with interconnected fibers. With an increasing amount of SiO_2, the 10 T/C sample retains partial fibrous and layered structures. In the 20 T/C sample, the fibrous structure gradually diminishes, transitioning into a complete sheet-like structure. Finally, the 30 T/C sample shows significant stacking and thickening between layers. The elemental mapping results indicate that no Si element is detected in pure chitosan. In contrast, the chitosan-silica hybrid demonstrates a clear and uniform distribution of Si on the surface. For the 30 T/C-5%B sample, which incorporates 5 wt% BG, particulate BG is visible on the material surface. In the early stages of synthesis, the acidic environment accelerates the diffusion of BG ions into the chitosan-silica hybrid matrix, resulting in a uniform distribution of Ca and P ions on the surface. During the subsequent synthesis process, dialysis is used to neutralize the environment, preserving the activity of the BG. The dispersion of Ca and P ions within the chitosan matrix potentially aids in direct cellular interaction.

In this study, the chitosan-silica hybrid was utilized as wound dressing. Apart from successfully employing a coupling agent to form covalent bonds between chitosan and silica, chitosan itself underwent 1-Ethyl-3-(3-dimethylaminopropyl)carbodiimide/N-Hydroxysuccinimide (EDC/NHS) treatment to generate chitosan conjugates. The principle of this treatment is as follows: firstly, the carboxylic acid group is activated by EDC to produce an O-acylisourea group; then, it is converted into a more stable active NHS-activated carboxylic acid group to form a primary amine (R-NH_2) with a carboxylic group (-COOH), ultimately resulting in the formation of an amide bond ($CONH_2$), thereby facilitating conjugation between chitosan molecules. This reaction significantly increases chitosan aggregation, thereby enhancing its swelling ratio [24]. In a previous study by Reyes-Peces et al. [25], GPTMS was also used to react with chitosan and silica to form a hybrid; however, they did not conjugate chitosan itself, resulting in only a modest 3.5-fold increase in swelling ratio. In contrast, in this experiment, as shown in Fig. 4(a), while pure chitosan becomes a mud-like substance after absorbing water, making it difficult to maintain its shape, the EDC/NHS crosslinking and coupling reactions transform the material into a soft and rubbery state [26], enabling precise measurement of its swelling ratio. The chitosan-silica hybrid samples exhibited a swelling ratio of approximately 17–19 times their dried weight. However, the standard deviations of all samples overlapped, making it difficult to determine which sample demonstrated the optimal swelling ratio. The swelling ratio experiment also revealed that water absorption behavior approaches saturation approximately 5 min after immersion in phosphate-buffered saline (PBS). Another important indicator of a wound dressing is water retention. When tissue fluid exudes from the wound, creating a moist environment at the wound site facilitates cell movement around the wound, aiding in cell repair. Therefore, many studies produce wound dressings in bilayer form to increase water retention [27]. 30 T/C exhibits a more complete layered structure compared to 10 T/C; moreover, the layers are not entirely solid, providing more water contact area and slightly enhancing the water retention rate compared to thinner fibers. On the other hand, the chitosan transitions into a viscous gel-like state, which helps water molecules remain more tightly retained within the structure. Compared to materials without specifically designed water-retaining structures, in experiments close to room temperature, collagen retains about 20 % after approximately 12 h, sodium lignosulfonate hydrogel retains approximately 64 % after around 6 h [28], and polyvinyl alcohol (PVA) based hydrogel retains approximately 65 % after about 7 h at 40 °C [29]. Although the chitosan-silica hybrid does not exhibit significant advantages in water retention, the material can still maintain over 46 % water retention after 8 h of experimentation, as shown in Fig. 4(b).

In terms of degradation rate, the results of the *in-vitro* experiments show that the chitosan-silica hybrid exhibits a slow degradation rate. In the 28-day *in-vitro* degradation experiment shown in Fig. 4(c). The

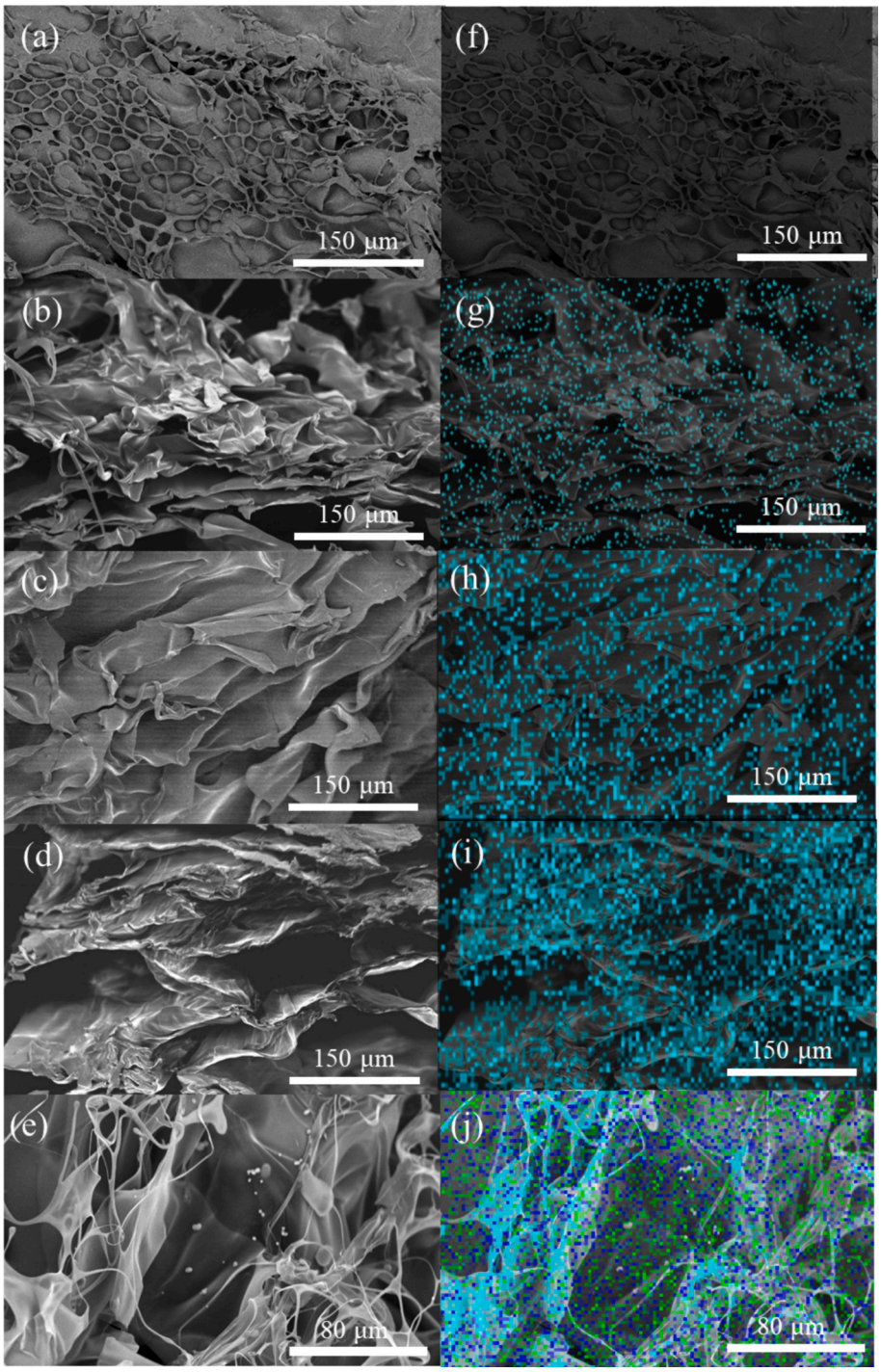

Fig. 3. (a–e) shows the SEM surface morphology of the chitosan-silica hybrid samples: (a) pure chitosan, (b) 10T/C, (c) 20T/C, (d) 30T/C, and (e) 30T/C-5%B. (f–j) represent the EDX elemental mapping corresponding to (a-e). It can be observed that with increasing TEOS content, the 30T/C dressing exhibits a thicker material compared to pure chitosan. The EDS elemental mapping indicates a homogeneous distribution of the Si element (cyan). Notably, in (j), the Ca element (green) and P element (blue) are also homogeneously distributed on the surface, suggesting the presence of Ca and P ions and BG distribution.

degradation behavior of chitosan varies with its degree of deacetylation [30]. Even chitosan with a deacetylation degree higher than 70 % can degrade slowly in a lysozyme-containing environment [31]. Although chitosan exhibits slow degradation rates over short periods, after approximately 6 to10 days, it becomes more soluble in water due to the protonation of its amino groups, which accelerates structural degradation and compromises stability [32]. Clinical studies have also observed that chitosan-based wound dressings are prone to cracking when dry and tend to become excessively gel-like in moist wound environments, altering their material properties and potentially reducing their effectiveness [33]. Similarly, in this study, chitosan was observed to dissolve in aqueous environments, forming a mud-like texture that renders it unsuitable as a stable wound dressing. In contrast, the material developed in this study, utilizing EDC/NHS crosslinking and coupling reactions, demonstrated highly uniform degradation characteristics. During the 28-day degradation experiment, no sudden acceleration of degradation occurred. Furthermore, the material did not exhibit brittleness in dry conditions and maintained its structural integrity without

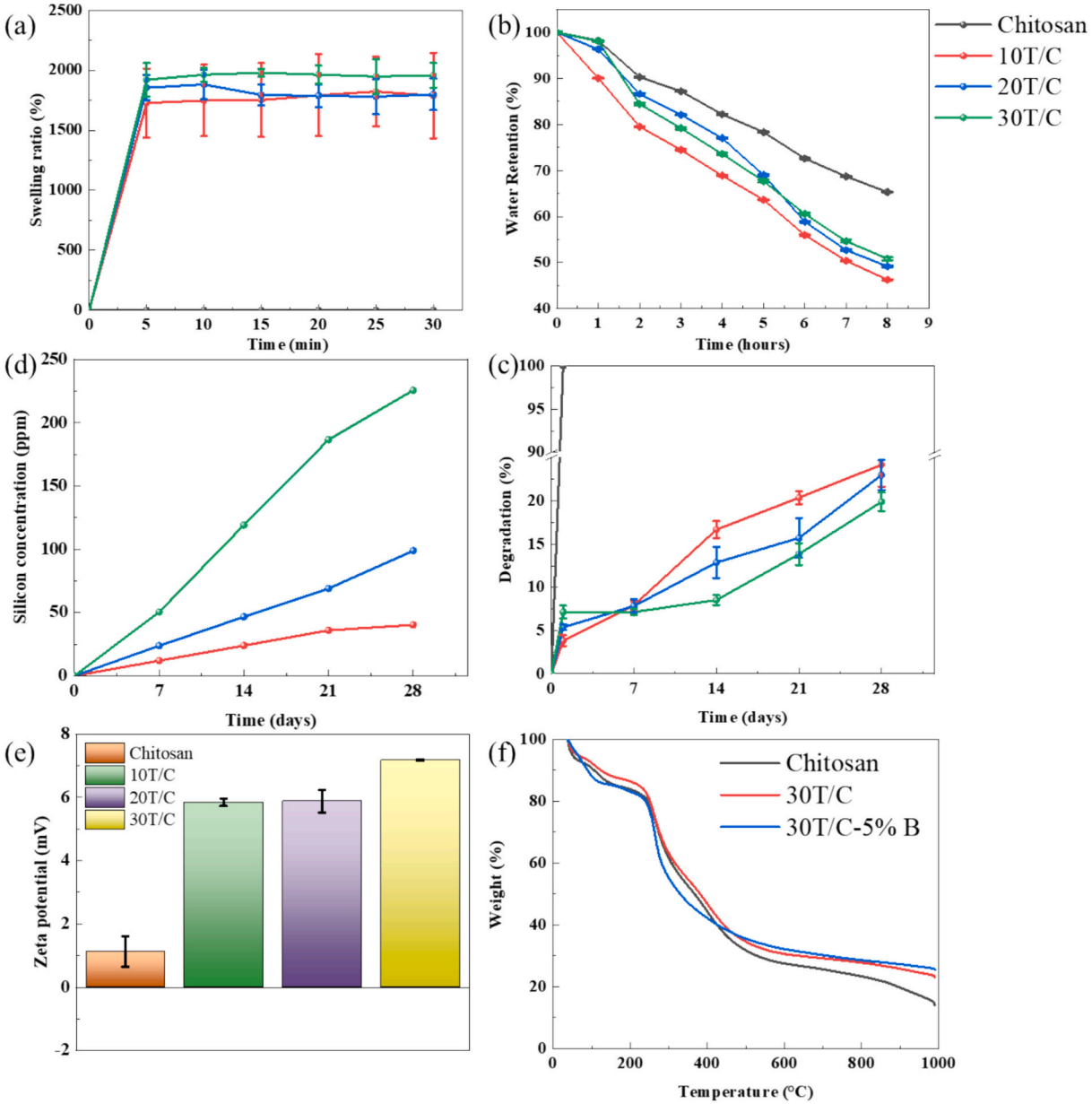

Fig. 4. (a) Swelling ratio, (b) water retention, (c) degradation, and (d) silicon ion release of chitosan and chitosan-silica hybrid. The above experiments were conducted by soaking samples in PBS. (e) Zeta potential for surface charge evaluation, and (f) TGA analysis for samples to evaluate organic and inorganic ratio.

forming uneven agglomerates when immersed in PBS. The degradation experiments for samples with low silica content, 10 T/C, showed approximately 24 wt% degradation after 28 days, while the 20 T/C sample showed 23 wt%, and the 30 T/C sample showed 20 wt%. Simultaneously, the release of silicon ions also increased with increasing silica concentration. In the 28-day degradation experiment, approximately 40 ppm of silicon ions were released from the 10 T/C sample, 99 ppm from the 20 T/C sample, and 226 ppm from the 30 T/C sample in Fig. 4(d). Although *in-vitro* experiments demonstrate slow degradation of the hybrid material, its degradation may accelerate in the more complex environment of an actual lesion. This could be influenced by individual variability and enzymatic activity, which may hasten material breakdown, potentially compromising the stability of the dressing. [2]. Additionally, Zeta potential was used to detect the surface charge of the material as shown in Fig. 4(e). Before measurement, the samples were soaked in PBS for 2 days to obtain the eluate. The chitosan showed a slightly positive charge of approximately 1.14 ± 0.48 mV. The surface charge of the samples increased with 10 T/C, 20 T/C, and 30 T/C, ranging from 5.84 ± 0.11, 5.88 ± 0.36, to 7.18 ± 0.02 mV, respectively. This is speculated to be due to the significant increase in surface charge caused by the hydrolysis of SiO_2 on the surface, leading to the generation of Si^{4+} ions in water. Based on the results of the above experiments, 30 T/C was selected for the incorporation of BG for the final biological experiments. Thermogravimetric analysis (TGA) was used to detect the concentration of inorganic materials within the samples. After high-temperature combustion, the chitosan left approximately 15 wt% of difficult-to-burn carbon compounds. Therefore, the remaining weight of 22 wt% for 30 T/C and 25 wt% for 30 T/C-5%B was determined to be the content of SiO_2 and BG, approximately 7 wt% and 3 wt%, respectively.

3.3. Cell viability and ALP activity

Cell viability was assessed using L929 cells for the preliminary examination of chitosan and chitosan-silica hybrid, as shown in Fig. 5(a). At a sample concentration of 1 mg/mL, all sample groups exhibited good cell viability. However, when the concentration of chitosan was

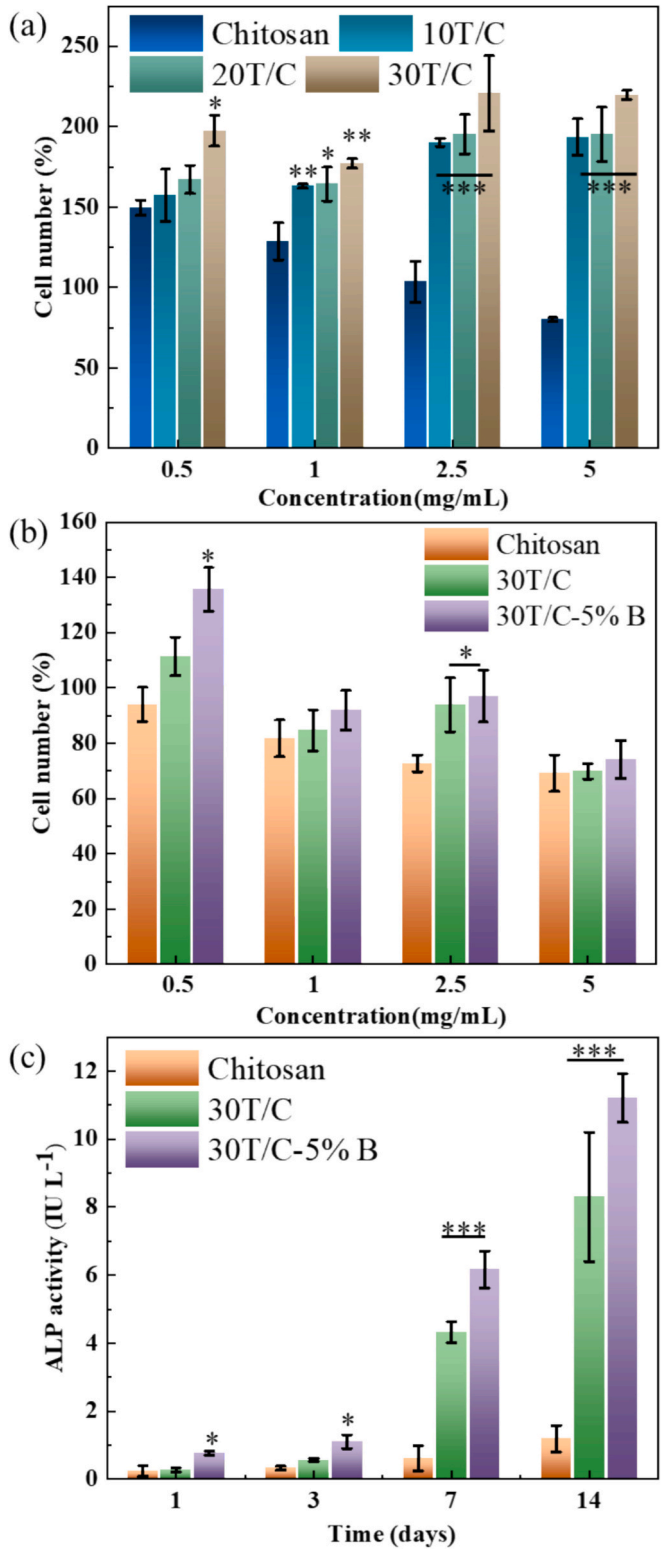

Fig. 5. *In-vitro* cell evaluations of samples. (a) Cell viability test using L929 cell line, (b) cell viability test using rBMSCs cell line, and (c) ALP activity test using rBMSCs cell line by co-culturing cells with "C" representing pure chitosan, 30T/C representing 10 wt% of TEOS in chitosan-silica hybrid, and 30T/C-5%B representing 5 wt% bioactive glass containing hybrid.

increased to 2.5 mg/mL, cell number began to decrease, from 149.6 ± 4.6 % at 0.5 mg/mL to 80.1 ± 1.2 %. Although cell viability remained above 80 %, it was evident that high concentrations of chitosan affected cell growth. On the other hand, in Fig. 5(b), rat bone mesenchymal stem cells (rBMSCs) were used to assess cell viability for the 30 T/C and 30 T/C-5%B samples. The results revealed a similar trend, with cell viability decreasing as sample concentration increased, reaching 69.1 ± 6.6 %, 69.8 ± 2.7 %, and 74.1 ± 6.8 % for C, 30 T/C, and 30 T/C-5%B, respectively, at a concentration of 5 mg/mL. Pure chitosan is well-known as a natural, non-toxic material that is safe for consumption and can be decomposed by gastric acid and enzymes in the gastrointestinal tract [34]. However, while chitosan is often reported as non-cytotoxic in various studies, this is contingent on factors such as Mw and concentration [35]. It is generally considered safe at concentrations in the μg/mL range, but previous research has shown that at higher concentrations in the mg/mL range, it can lead to necrotic or autophagic cell death. This may be attributed to the positively charged chitosan being phagocytosed by cells, resulting in cell membrane damage and subsequent enzyme leakage [36]. In contrast, the more complete structure of 30 % T/C prevents phagocytosis, thereby reducing cell death. Additionally, the incorporation of 5 % BG in 30 T/C enhances its properties. BG rapidly releases alkaline ions upon contact with water, creating an alkaline environment [37]. This, combined with the hybrid's reinforcing effect, stabilizes the material's structure, contributing to its higher bioactivity. Alkaline phosphatase (ALP) is a widely recognized early marker of osteogenic differentiation, reflecting the commitment of rBMSCs toward the osteoblastic lineage. In this study, ALP activity was used to evaluate the osteogenic potential of bioactive glass-containing materials, as ALP is responsible for generating inorganic phosphate to support initial matrix mineralization. Consistent with previous findings by Meng et al. [38], ALP expression is upregulated during early differentiation and is sensitive to variations in BG composition, particularly calcium content. Therefore, ALP serves as a reliable and responsive indicator of osteogenic induction, especially during the early phase of differentiation. In Fig. 5(c), ALP activity was tested by co-culturing the materials with rBMSCs for 1, 3, 7, and 14 days to observe trends in ALP activity. There are many factors influencing ALP activity, among which chitosan-silica hybrids exhibit higher ALP activity than chitosan. Previous studies by Schröder et al. [39] indicated that co-culturing silica/silicate with SaOS-2 human osteosarcoma cell line and RAW 264.7 macrophage cells at concentrations ranging from 0 to 100 μM can alter the expression of OPG and RANKL genes, thereby inhibiting the differentiation and growth of RAW 264.7 into osteoclast-like cells while promoting osteoblast differentiation [39] As shown in Fig. 4(d), 30 T/C released a certain amount of Si species at different time points, and other studies have also mentioned that the presence of Si^{4+} can increase the gene expressions of osteogenesis and cementogenesis, as well as ALP activity [40]. In Fig. 4(e), the zeta potential results also correspondingly showed higher positive charges in the eluate. For the 30 T/C-5%B sample, ALP activity exceeded that of 30 T/C, possibly due to the presence of not only Si^{4+} but also Ca^{2+} ions released by BG, along with mineralized nodules formed by PO_4^{3-} and CO_3^{2-}, which combinatorically regulate osteoblast OCN expression and biomineralization [41]. These *in-vitro* results also support subsequent cranial defect experiments.

3.4. Wound healing assay

Wound healing involves a highly complex process simplified into four stages: 1. Hemostasis, 2. Inflammation, 3. Proliferation, and 4. Remodeling [42]. However, wound healing requires various cells to participate in activities. Wound healing assays necessitate significant cellular involvement, particularly during the initial stages of wound formation, where fibroblasts must establish thorough cell-surface interactions before accelerating migration into the cell-free area. The faster the cell migration speed, the quicker cell-cell as well as cell-matrix interactions can form within the first hours of wound healing,

highlighting the crucial importance of wound dressing in facilitating interactions between cells and the wound site [43]. In Fig. 6, it is evident that in the control group, cells slowly move toward the central cell-free area after 4 h of experimentation. In contrast, both chitosan and chitosan-silica hybrids exhibit a small number of cells in the blank area. At the same time, 30 T/C-5%B shows a significant number of cells already moving toward the central blank area, with fibroblast filopodia extending in all directions. This demonstrates good interaction between cells and the material, promoting radially uniform cell outgrowths and distribution of nuclei [44]. Subsequent experiments at 12 and 24 h further illustrate that 30 T/C and 30 T/C-5%B contribute to cell migration.

3.5. *In-vivo wound healing experiment and histological analysis*

In Fig. 7(a), an *in-vivo* wound healing experiment was conducted, where materials were directly applied to the wound site and fixed without any further treatment to observe wound healing progress. The results of the 7-day experiment indicate that the chitosan-silica hybrid has not fully degraded at the wound site. By day 14, significant wound closure was observed; subsequently, all groups exhibited complete wound closure by day 21 of the experiment. In the animal experiments, Fig. 7(b) shows that the chitosan-silica hybrid group exhibited slight improvement in wound healing compared to the control group. Although the chitosan-silica hybrid did not demonstrate significant skin repair effects, an improvement in wound healing was observed on days 7 and 14.

Subsequently, samples from each time point were subjected to Masson's trichrome staining to analyze collagen, connective tissue, and surrounding soft tissue repair, as depicted in Fig. 7(c). It was notably observed in the 7-day samples that the control group exhibited more cells and cytoplasm at the wound site. In comparison, the samples from the 30 T/C and 30 T/C-5%B groups demonstrated more pronounced collagen formation and angiogenesis at the wound site, indicating faster wound repair progress. By day 14 of the experiment, the control samples exhibited the formation of numerous small blood vessels. However, the other two samples showed blood vessel formation by day 7, with larger blood vessels and more pronounced collagen formation observed by day 14. The results from these histological sections are consistent with the direct observation of wound closure process. Both 30 T/C and 30 T/C-5%B have demonstrated efficacy in assisting wound healing.

3.6. *Liver injury hemostasis study*

Hemostasis is one of the crucial functions of wound dressing. As mentioned earlier, the primary key to wound repair lies in hemostasis, which involves a complex physiological process, from the initial platelet response causing platelet adhesion to collagen in blood vessels, forming a blockage and subsequent clotting [45], to the body's response to the wound stimulus, releasing thromboxane and epinephrine, leading to vasoconstriction and reduced bleeding, involving a series of coagulation factors [46].

This study used gauze as a control group to compare the effects of chitosan-silica hybrid on hemostasis, as shown in Fig. 8. Gauze took 124.5 ± 10.6 s to absorb 973.0 ± 34.6 mg of blood before hemostasis, compared to 68.5 ± 10.6 s and 53.5 ± 13.4 s for 30 T/C and 30 T/C-5% B, which absorbed 609.0 ± 25.5 mg and 247.3 ± 21.7 mg of blood, respectively, before hemostasis. 30 T/C-5%B exhibits a significantly better hemostatic effect. Chitosan, silica, and BG play essential roles in the hemostasis process. Previous studies have indicated that chitosan application to the wound site can increase the secretion of hyaluronic acid [47] while also attracting platelets and plasma proteins around the

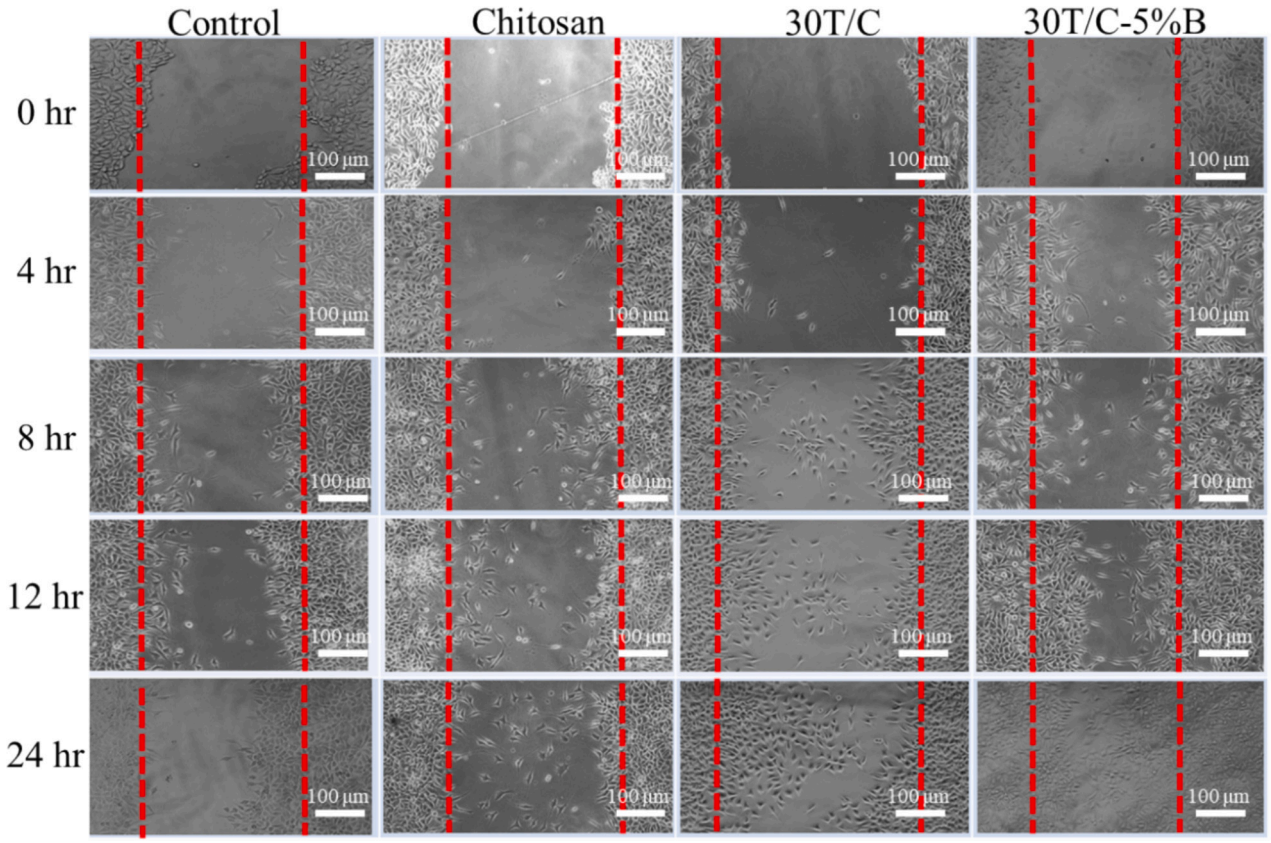

Fig. 6. *In-vitro* wound healing assay was conducted to observe cell migration behavior in the presence of material extraction, simulating cell interaction between the wound and the material. The red dashed line represents the scratch region generated using a 1000 μL pipette tip to observe cell migration speed after co-culture for 0, 4, 8, 12, and 24 h.

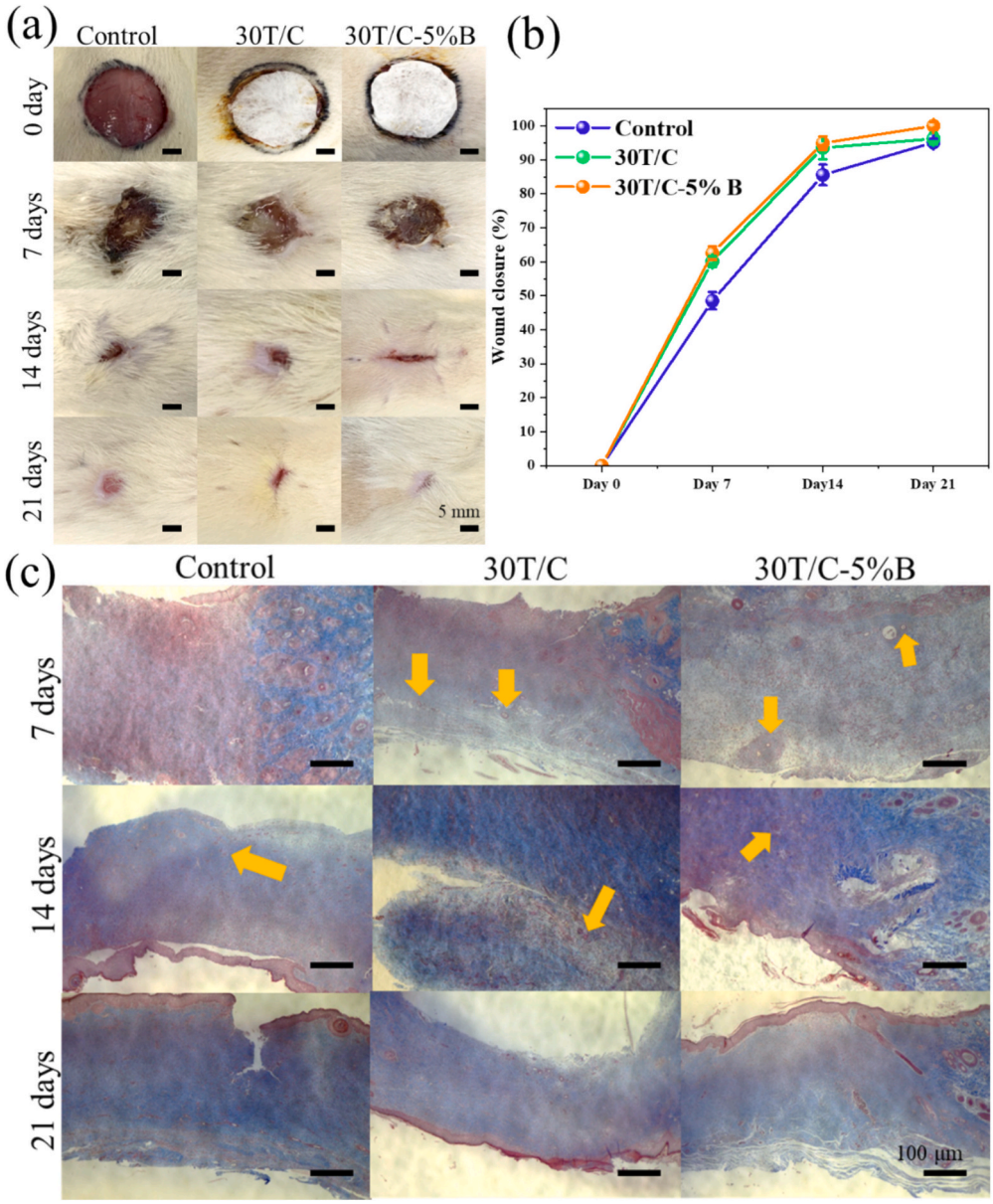

Fig. 7. (a) *In-vivo* wound healing experiment involved cutting samples into circular wounds with a diameter of 2.5 cm. Samples were observed at 0, 7, 14, and 21 days to assess their wound healing and degradation performance. (b) Wound healing trend graph. (c) Tissue histological analysis from the experimental groups observed in (c) were stained with Masson's trichrome stain to examine the regeneration of collagen and connective tissue. Yellow arrows indicate newly formed blood vessels.

wound to induce blood clotting and vasoconstriction at the injured site [48]. Furthermore, as a naturally positively charged polymer, chitosan enhances coagulation by attracting negatively charged cells in the blood, such as red blood cells and platelets. Additionally, when the chitosan-silica hybrid comes into contact with blood, it generates more positive charges, as shown in Fig. 4(e), which aids in enhancing the clotting process. In previous studies, dynamic degradation experiments were conducted on various BGs. When exposed to Tris buffer solution, all BGs rapidly released Si, Ca, and P ions, showing a sharp maximum at early time points (approximately 50 to 100 s) [49]. Therefore, it is hypothesized that in the case of 30 T/C-5%B, the presence of numerous cations, such as Si^{4+} and Ca^{2+}, in the chitosan-silica hybrid matrix enhances the coagulation process [50,51].

3.7. Cranial defect experiment and histological analysis

Fig. 9 displays the computed tomography (CT) reconstructed images of skull defects at 2 and 4 weeks, with the area reduction calculated using Image J software. In the 2-week CT images, it is evident that the defects in the control and 30 T/C groups did not show significant BV/TV ratio, approximately 8.8 ± 2.4 % and 7.2 ± 3.3 %, respectively. However, in the 30 T/C-5%B group, irregular new bone formation is observable at the edge of the bone defect, achieving a 60.3 ± 3.8 % in area. In the 4-week experiment, slight new bone or partially mineralized collagen tissue formation is observed around the control group, accounting for approximately 30.6 ± 8.1 %. The 30 T/C group shows a 26.2 ± 7.8 %, but due to individual differences, there was no significant bone regeneration differences observed compared to the control group. Although 30 T/C demonstrated better performance in soft tissue wound healing compared to the control, it did not provide significant assistance in bone healing. On the other hand, the 30 T/C-5%B samples, incorporating a certain amount of BG, exhibited relatively faster bone healing, reaching 77.1 ± 6.7 % new bone formation after 4 weeks. Previous studies have indicated that BG, due to its composition containing a large

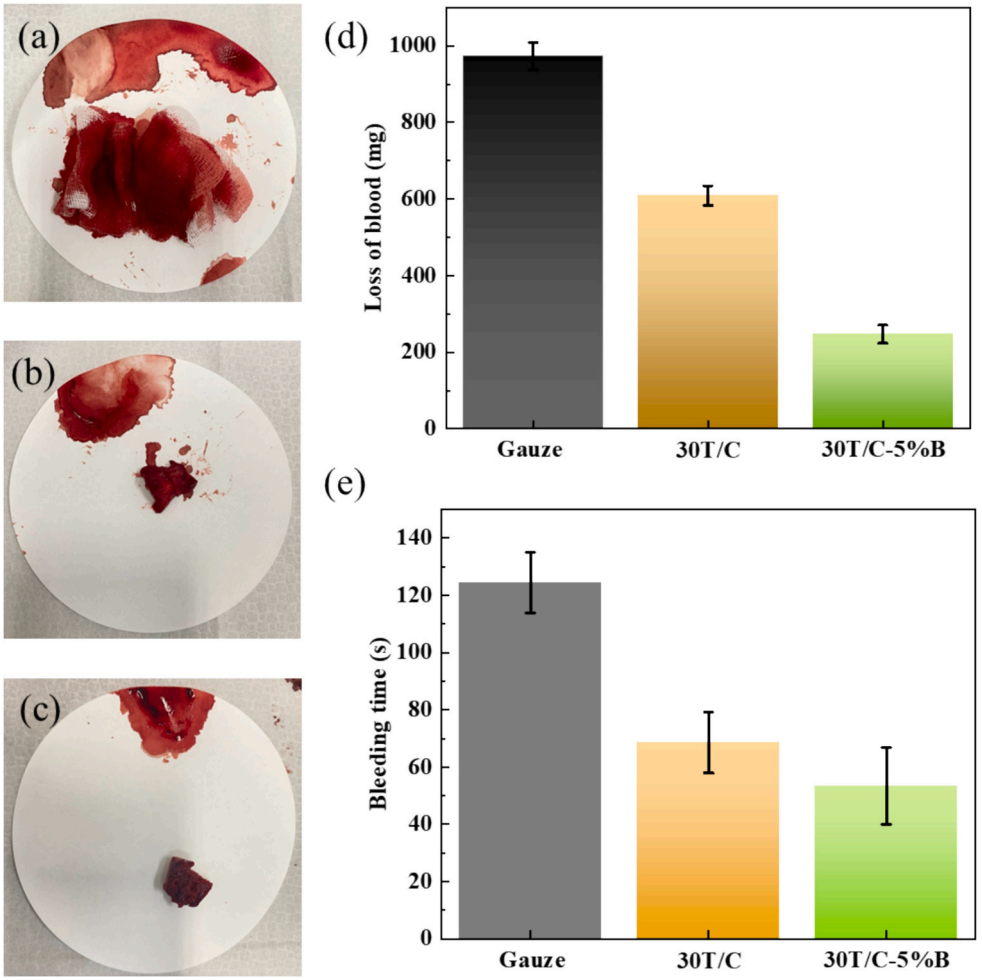

Fig. 8. The liver injury hemostasis experiments have been performed using the SD rat model. The SD rat liver was moved from the abdominal cavity and placed on a 47 mm filter with a 5 mm diameter biopsy punch, creating a wound approximately 5 mm in depth. Subsequently, (a) gauze, (b) 30T/C, and (c) 30T/C-5%B dressing were gently placed on the wound without additional pressure applied, and hemostasis was observed. Concurrently, (d) blood weight and (e) bleeding time were recorded.

amount of Ca and P ions, creates a locally high concentration of ions when implanted in the body, leading to the differentiation of mesenchymal stem cells into osteoblasts, thereby depositing and mineralizing new bone [17,52].

Subsequently, the samples underwent histological staining (Hematoxylin and eosin (H&E) staining and Masson's trichrome staining), as shown in Fig. 10. No significant inflammatory response was observed in any of the samples. Corresponding to the H&E and Masson's trichrome staining results within the yellow and green circles in figures, in the 2-week samples, slight collagen aggregation and a trend toward ossification were observed in the 30 T/C samples, while significant new bone formation was observed around the skull defect in the 30 T/C-5%B samples. Conversely, the control group tissues tended to grow from the edge of the skull defect. By the 4-week, the 30 T/C samples were encapsulated by fibrous tissue, with evident infiltration of blood cells into the material structure, along with some new bone formation and more collagen aggregation. On the other hand, the 30 T/C-5%B samples exhibited significantly more complete bone formation, growing around the skull defect as a layer of new bone formed from collagen and fibrous tissue. Although gaps remained between the bones, the integrity of ossification was high, with the material interior filled with cells, primarily mineralizing collagen tissue, and a high degree of fibrous tissue and blood vessels surrounding the material. These results indicate that chitosan-silica hybrid, after incorporating BG, can significantly aid in bone repair.

4. Conclusions

This study introduces a multifunctional wound healing material in the form of a chitosan-silica wound dressing. Through a coupling reaction, the dressing forms a covalent bond between chitosan and silica networks, enhancing its structural stability and reducing degradation. Pre-treatment of chitosan with polymerization maintains its swelling ability and combines with its inherent positive charges and silica network hydrolyzed Si^{4+} ions, further enhancing hemostasis. In wound healing experiments, the chitosan-silica hybrid demonstrates significant efficacy, while the incorporation of BG accelerates bone regeneration. This dressing holds promise for addressing chronic wounds involving soft tissue and bone defects, providing properties such as hemostasis, lower inflammatory response, wound healing assistance, bone remodeling, and slow degradation, suitable for a wide range of applications.

CRediT authorship contribution statement

Yu-Chien Lin: Writing – review & editing, Writing – original draft, Methodology, Formal analysis, Data curation, Conceptualization. **Susaritha Ramanathan:** Writing – original draft, Data curation. **Huey-Yuan Wang:** Methodology, Investigation, Funding acquisition. **Ying-Chun Lin:** Methodology, Data curation. **Wai-Ching Liu:** Methodology, Formal analysis. **Julian R. Jones:** Supervision, Formal analysis. **Nam-Joon Cho:** Writing – original draft, Supervision, Resources, Funding

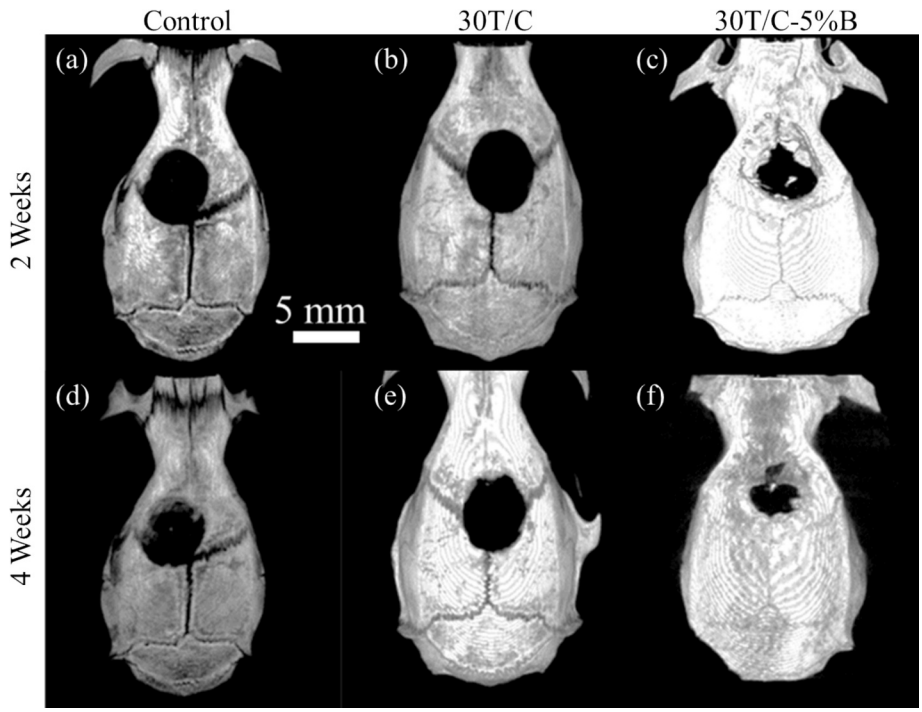

Fig. 9. The cranial defect repair experiment is divided into three groups: (a) and (d) represent the empty control group, (b) and (e) represent the 30 T/C group, and (c) and (f) represent the 30T/C-5%B group. CT reconstruction images are shown for 2 weeks (W2) and 4 weeks (W4) after implantation of the materials.

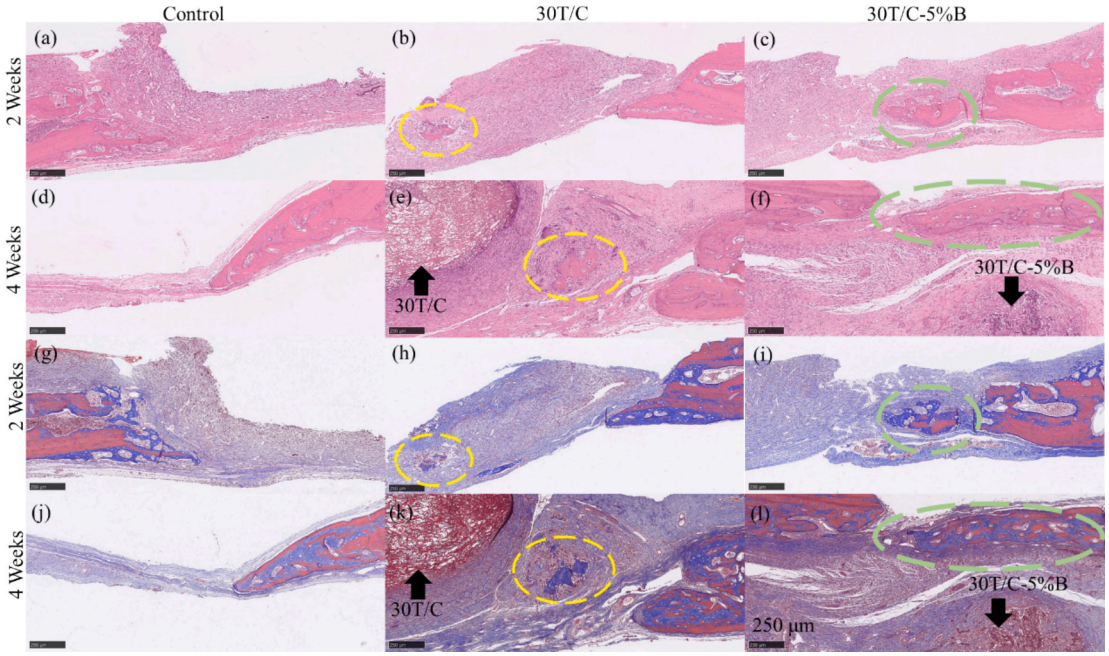

Fig. 10. The histological analysis of the cranial defect repair experiment. (a–f) H&E staining and (g–l) Masson's trichrome staining. The yellow and green dashed lines in the images indicate corresponding locations. It can be observed that 30T/C exhibits a higher density of collagen accumulation and is trending toward ossification. In the samples of 30T/C-5%B, more collagen aggregation and a significant amount of new bone formation can be observed.

acquisition, Formal analysis, Conceptualization. **Chih-Chien Hu:** Supervision, Resources, Methodology, Investigation. **Ren-Jei Chung:** Writing – review & editing, Supervision, Funding acquisition, Conceptualization.

Declaration of competing interest

The authors declare that they have no known competing financial interests or personal relationships that could have appeared to influence the work reported in this paper.

Acknowledgments

The authors are grateful for the financial support received from the National Science and Technology Council of Taiwan (NSTC 111-2622-E-027-022; NSTC 112-2622-E-027-020; NSTC 112-2314-B-182A-102-

MY2); and the National Taipei University of Technology-Mackay Memorial Hospital Joint Research Program (NTUT-MMH-113-03). Technical assistance from the Precision Analysis and Material Research Center of the National Taipei University of Technology (Taipei Tech) is appreciated. In addition, this work was financially supported by the Tier 3 program (grant no. MOET32022-0008) and was also supported by the Cellular Agriculture Programme (CellAg) grant REQ414940 awarded by National Research Foundation, Singapore under its Campus for Research Excellence and Technological Enterprise (CREATE) program and Ministry of Education (MOE) grant MOE-MOET32022-0002. The authors also thank their colleagues in the Translational Materials Innovation Group (TMIG) and the Centre for Cross Economy.

X-ray images assistance from the Taiwan Mouse Clinic (TMC) is appreciated. All animal experiments and care were ethically approved by Laboratory Animal Center of Taipei Medical University (LAC-2022-0203) and Chang Gung Memorial Hospital, Linkou (IACUC No: 2023030305).

Data availability

Data will be made available on request.

References

[1] G. FrykbergRobert, Challenges in the treatment of chronic wounds, Adv. Wound Care 4 (9) (2015) 513–582.
[2] R. Laurano, M. Boffito, G. Ciardelli, V. Chiono, Wound dressing products: a translational investigation from the bench to the market, Engineered Regeneration 3 (2) (2022) 182–200.
[3] E. Madadian, E. Naseri, R. Legault, A. Ahmadi, Development of 3D-printable albumin–alginate foam for wound dressing applications, 3D Print. Addit. Manuf. 11 (3) (2024) 907–918.
[4] N. Asadi, H. Pazoki-Toroudi, A.R. Del Bakhshayesh, A. Akbarzadeh, S. Davaran, N. Annabi, Multifunctional hydrogels for wound healing: special focus on biomacromolecular based hydrogels, Int. J. Biol. Macromol. 170 (2021) 728–750.
[5] Y. Zhang, Y. Wang, Y. Li, Y. Yang, M. Jin, X. Lin, Z. Zhuang, K. Guo, T. Zhang, W. Tan, Application of collagen-based hydrogel in skin wound healing, Gels 9 (3) (2023) 185.
[6] J.U. Park, H.D. Jung, E.H. Song, T.H. Choi, H.E. Kim, J. Song, S. Kim, The accelerating effect of chitosan-silica hybrid dressing materials on the early phase of wound healing, J Biomed Mater Res B Appl Biomater 105 (7) (2017) 1828–1839.
[7] J. Peng, H. Zhao, C. Tu, Z. Xu, L. Ye, L. Zhao, Z. Gu, D. Zhao, J. Zhang, Z. Feng, In situ hydrogel dressing loaded with heparin and basic fibroblast growth factor for accelerating wound healing in rat, Mater. Sci. Eng. C 116 (2020) 111169.
[8] J.-S. Oh, E.-J. Lee, Engineered dressing of hybrid chitosan-silica for effective delivery of keratin growth factor and acceleration of wound healing, Mater. Sci. Eng. C 103 (2019) 109815.
[9] X. Liu, H.-H. Chen, Y.-C. Lin, S.C. Nabilla, W.-C. Liu, W.-C. Wang, S.-J. Shih, Y. Li, C.-P. Lin, G. Zhao, Composite polyelectrolyte multilayer and mesoporous bioactive glass nanoparticle coating on 316L stainless steel for controlled antibiotic release and biocompatibility, J. Biomed. Nanotechnol. 14 (4) (2018) 725–735.
[10] D. Ailincai, M. Bercea, I. Rosca, I. Sandu, L. Marin, Antimicrobial chitosan-based hydrogels: a novel approach to obtain sanitizers, Carbohydr. Polym. 354 (2025) 123288–123305.
[11] X. Wang, X. Zhang, W. Zhao, L. Zhu, L. Hong, K. Cui, N. Yu, Z. Chen, M. Wen, Chitosan-based hydrogel incorporated with polydopamine and protoporphyrin for photothermal-oxidation sterilization of bacteria-infected wound therapy, J. Colloid Interface Sci. 678 (2025) 89–100.
[12] Z. Pang, Y. Yao, Z. Xu, K. Liu, X. Wu, X. Zhang, H. Dai, Natural polymer chitosan-based hydrogels can enhance mechanical properties and produce H2S gas by UV-light to treat scalded wound, Int. J. Biol. Macromol. 306 (2025) 141289.
[13] Y.C. Lin, C.Y. Lee, J.R. Jones, W.C. Liu, N.J. Cho, C.C. Hu, R.J. Chung, Sustained antibiotic release from biodegradable gelatin–silica hybrid for orthopedic infections, Adv. Funct. Mater. 34 (49) (2024) 2409491–2409504.
[14] S. Pandey, S.B. Mishra, Sol–gel derived organic–inorganic hybrid materials: synthesis, characterizations and applications, J. Sol-Gel Sci. Technol. 59 (2011) 73–94.
[15] Y.-C. Lin, H.-Y. Wang, Y.-C. Tang, W.-R. Lin, C.-L. Tseng, C.-C. Hu, R.-J. Chung, Enhancing wound healing and adhesion through dopamine-assisted gelatin-silica hybrid dressings, Int. J. Biol. Macromol. 258 (2024) 128845.
[16] E.M. Valliant, J.R. Jones, Softening bioactive glass for bone regeneration: sol–gel hybrid materials, Soft Matter 7 (11) (2011) 5083–5095.
[17] S.J. Shih, D.R.M. Sari, Y.C. Lin, Influence of chemical composition on the bioactivity of spray pyrolyzed mesoporous bioactive glass, Int. J. Appl. Ceram. Technol. 13 (4) (2016) 787–794.
[18] Y.-C. Lin, G. Young, H. Iqbal, A.I. Kondarage, A. Karunaratne, J.R. Jones, F. Tallia, Effect of process variables on optimization of mechanical properties of silica/poly (tetrahydrofuran) sol-gel hybrids, J. Sol-Gel Sci. Technol. (2025) 1–15.
[19] S.-J. Shih, B.-J. Hong, Y.-C. Lin, Novel graphene oxide-containing antibacterial mesoporous bioactive glass, Ceram. Int. 43 (2017) S784–S788.
[20] L. Gabrielli, L. Connell, L. Russo, J. Jiménez-Barbero, F. Nicotra, L. Cipolla, J. R. Jones, Exploring GPTMS reactivity against simple nucleophiles: chemistry beyond hybrid materials fabrication, RSC Adv. 4 (4) (2014) 1841–1848.
[21] S.S. Silva, R.A. Ferreira, L. Fu, L.D. Carlos, J.F. Mano, R.L. Reis, J. Rocha, Functional nanostructured chitosan–siloxane hybrids, J. Mater. Chem. 15 (35–36) (2005) 3952–3961.
[22] X. Li, D. Zeng, P. Ke, G. Wang, D. Zhang, Synthesis and characterization of magnetic chitosan microspheres for drug delivery, RSC Adv. 10 (12) (2020) 7163–7169.
[23] N. Mabungela, N.D. Shooto, F. Mtunzi, E.B. Naidoo, M. Mlambo, K.E. Mokubung, S. Mpelane, Multi-application of fennel (Foeniculum vulgaris) seed composites for the adsorption and photo-degradation of methylene blue in water, South African Journal of Chemical Engineering 44 (1) (2023) 283–296.
[24] Y. Qin, P. Li, Antimicrobial chitosan conjugates: current synthetic strategies and potential applications, Int. J. Mol. Sci. 21 (2) (2020) 499.
[25] M.V. Reyes-Peces, A. Pérez-Moreno, D.M. de-Los-Santos, M.d.M. Mesa-Díaz, G. Pinaglia-Tobaruela, J.I. Vilches-Pérez, R. Fernández-Montesinos, M. Salido, N. de la Rosa-Fox, M. Piñero, Chitosan-GPTMS-silica hybrid mesoporous aerogels for bone tissue engineering, Polymers 12 (11) (2020) 2723, https://doi.org/10.3390/polym12112723.
[26] B. Kaczmarek, A. Sionkowska, J. Kozlowska, A. Osyczka, New composite materials prepared by calcium phosphate precipitation in chitosan/collagen/hyaluronic acid sponge cross-linked by EDC/NHS, Int. J. Biol. Macromol. 107 (2018) 247–253.
[27] M. Li, Y. Dong, M. Wang, X. Lu, X. Li, J. Yu, B. Ding, Hydrogel/nanofibrous membrane composites with enhanced water retention, stretchability and self-healing capability for wound healing, Compos. Part B Eng. 257 (2023) 110672.
[28] X. Wang, Y. Wang, S. He, H. Hou, C. Hao, Ultrasonic-assisted synthesis of superabsorbent hydrogels based on sodium lignosulfonate and their adsorption properties for Ni2+, Ultrason. Sonochem. 40 (2018) 221–229.
[29] X. Wang, H. Hou, Y. Li, Y. Wang, C. Hao, C. Ge, A novel semi-IPN hydrogel: preparation, swelling properties and adsorption studies of Co (II), J. Ind. Eng. Chem. 41 (2016) 82–90.
[30] J. Zhao, P. Qiu, Y. Wang, Y. Wang, J. Zhou, B. Zhang, L. Zhang, D. Gou, Chitosan-based hydrogel wound dressing: from mechanism to applications, a review, Int. J. Biol. Macromol. 244 (2023) 125250.
[31] Y. Yang, W. Hu, X. Wang, X. Gu, The controlling biodegradation of chitosan fibers by N-acetylation in vitro and in vivo, J. Mater. Sci. Mater. Med. 18 (2007) 2117–2121.
[32] Y. Kong, X. Tang, Y. Zhao, X. Chen, K. Yao, L. Zhang, Q. Han, L. Zhang, J. Ling, Y. Wang, Degradable tough chitosan dressing for skin wound recovery, Nanotechnol. Rev. 9 (1) (2020) 1576–1585.
[33] R.A. Muzzarelli, P. Morganti, G. Morganti, P. Palombo, M. Palombo, G. Biagini, M. M. Belmonte, F. Giantomassi, F. Orlandi, C. Muzzarelli, Chitin nanofibrils/chitosan glycolate composites as wound medicaments, Carbohydr. Polym. 70 (3) (2007) 274–284.
[34] B.R. Rizeq, N.N. Younes, K. Rasool, G.K. Nasrallah, Synthesis, bioapplications, and toxicity evaluation of chitosan-based nanoparticles, Int. J. Mol. Sci. 20 (22) (2019) 5776.
[35] A. Matica, G. Menghiu, V. Ostafe, Toxicity of chitosan-based products, New Front. Chem. 26 (1) (2017).
[36] J.W. Loh, G. Yeoh, M. Saunders, L.-Y. Lim, Uptake and cytotoxicity of chitosan nanoparticles in human liver cells, Toxicol. Appl. Pharmacol. 249 (2) (2010) 148–157.
[37] T. Mehrabi, A.S. Mesgar, Z. Mohammadi, Bioactive glasses: a promising therapeutic ion release strategy for enhancing wound healing, ACS Biomater Sci. Eng. 6 (10) (2020) 5399–5430.
[38] L. Meng, P. Zhao, Y. Jiang, J. You, Z. Xu, K. Yu, A.R. Boccaccini, J. Ma, K. Zheng, Extracellular and intracellular effects of bioactive glass nanoparticles on osteogenic differentiation of bone marrow mesenchymal stem cells and bone regeneration in zebrafish osteoporosis model, Acta Biomater. 174 (2024) 412–427.
[39] H. Schröder, X. Wang, M. Wiens, B. Diehl-Seifert, K. Kropf, U. Schloßmacher, W. Müller, Silicate modulates the cross-talk between osteoblasts (SaOS-2) and osteoclasts (RAW 264.7 cells): inhibition of osteoclast growth and differentiation, J. Cell. Biochem. 113 (10) (2012) 3197–3206.
[40] N. Mei, Y. Wu, B. Chen, T. Zhuang, X. Yu, B. Sui, T. Ding, X. Liu, 3D-printed mesoporous bioactive glass/GelMA biomimetic scaffolds for osteogenic/cementogenic differentiation of periodontal ligament cells, Front. Bioeng. Biotechnol. 10 (2022) 950970.
[41] N.S. Tousi, M.F. Velten, T.J. Bishop, K.K. Leong, N.S. Barkhordar, G.W. Marshall, P. M. Loomer, P.B. Aswath, V.G. Varanasi, Combinatorial effect of Si^{4+}, Ca^{2+}, and Mg^{2+} released from bioactive glasses on osteoblast osteocalcin expression and biomineralization, Mater. Sci. Eng. C 33 (5) (2013) 2757–2765.
[42] E.M. Tottoli, R. Dorati, I. Genta, E. Chiesa, S. Pisani, B. Conti, Skin wound healing process and new emerging technologies for skin wound care and regeneration, Pharmaceutics 12 (8) (2020) 735.
[43] G. Shabestani Monfared, P. Ertl, M. Rothbauer, An on-chip wound healing assay fabricated by xurography for evaluation of dermal fibroblast cell migration and wound closure, Sci. Rep. 10 (1) (2020) 16192.
[44] H.L. Hiraki, D.L. Matera, M.J. Rose, R.N. Kent, C.W. Todd, M.E. Stout, A.E. Wank, M.C. Schiavone, S.J. DePalma, A.A. Zarouk, Magnetic alignment of electrospun fiber segments within a hydrogel composite guides cell spreading and migration phenotype switching, Front. Bioeng. Biotechnol. 9 (2021) 679165.

[45] M.N. Sundaram, U. Mony, P.K. Varma, J. Rangasamy, Vasoconstrictor and coagulation activator entrapped chitosan based composite hydrogel for rapid bleeding control, Carbohydr. Polym. 258 (2021) 117634.
[46] C. Toonstra, Y. Hu, H. Zhang, Deciphering the roles of N-glycans on collagen–platelet interactions, J. Proteome Res. 18 (6) (2019) 2467–2477.
[47] Y. Liu, H. Niu, C. Wang, X. Yang, W. Li, Y. Zhang, X. Ma, Y. Xu, P. Zheng, J. Wang, Bio-inspired, bio-degradable adenosine 5′-diphosphate-modified hyaluronic acid coordinated hydrophobic undecanal-modified chitosan for hemostasis and wound healing, Bioactive Materials 17 (2022) 162–177.
[48] S.O. Ebhodaghe, A short review on chitosan and gelatin-based hydrogel composite polymers for wound healing, J. Biomater. Sci. Polym. Ed. 33 (12) (2022) 1595–1622.
[49] R. Brückner, M. Tylkowski, L. Hupa, D.S. Brauer, Controlling the ion release from mixed alkali bioactive glasses by varying modifier ionic radii and molar volume, J. Mater. Chem. B 4 (18) (2016) 3121–3134.
[50] P. Fan, Y. Zeng, D. Zaldivar-Silva, L. Agüero, S. Wang, Chitosan-based hemostatic hydrogels: the concept, mechanism, application, and prospects, Molecules 28 (3) (2023) 1473.
[51] J. Turner, A. Nandakumar, N. Anilbhai, A. Boccaccini, J. Jones, G. Jell, The effect of Si species released from bioactive glasses on cell behaviour: a quantitative review, Acta Biomater. 170 (2023) 39–52.
[52] J.R. Jones, Review of bioactive glass: from Hench to hybrids, Acta Biomater. 9 (1) (2013) 4457–4486.